35. M. H. Begemann, R. J. Saykally, *J. Chem. Phys.* **82**, 3570 (1985).
36. M. Gruebele, M. Polak, R. J. Saykally, *J. Chem. Phys.* **87**, 3347 (1987).
37. That all of the larger clusters display sharp absorption near 1600 cm^{-1} demonstrates that the Ar atom is sufficiently weakly bound to enable action spectroscopy at this low excitation energy, thereby eliminating earlier uncertainties relating to photofragmentation kinetics.
38. Y.-S. Wang *et al.*, *J. Phys. Chem. A* **107**, 4217 (2003).
39. C.-K. Lin *et al.*, *Phys. Chem. Chem. Phys.* **7**, 938 (2005).
40. C. V. Ciobanu, L. Ojamae, I. Shavitt, S. J. Singer, *J. Chem. Phys.* **113**, 5321 (2000).

41. M.A.D., M.A.J., and K.D.J. thank the NSF for their support under grant numbers 0244143, 0111245, and 0078528.

4 April 2005; accepted 5 May 2005
10.1126/science.1113094

The Size and Duration of the Sumatra-Andaman Earthquake from Far-Field Static Offsets

P. Banerjee,[1] F. F. Pollitz,[2] R. Bürgmann[3]*

The 26 December 2004 Sumatra earthquake produced static offsets at continuously operating GPS stations at distances of up to 4500 kilometers from the epicenter. We used these displacements to model the earthquake and include consideration of the Earth's shape and depth-varying rigidity. The results imply that the average slip was >5 meters along the full length of the rupture, including the ~650-kilometer-long Andaman segment. Comparison of the source derived from the far-field static offsets with seismically derived estimates suggests that 25 to 35% of the total moment release occurred at periods greater than 1 hour. Taking into consideration the strong dip dependence of moment estimates, the magnitude of the earthquake did not exceed M_w = 9.2.

The 26 December 2004 Sumatra-Andaman earthquake was the largest seismic event to strike in the era of modern space geodesy. This event apparently ruptured a >1200-km section of the megathrust in a complex sequence of rapid and slow slip episodes that lasted for more than 1000 s (*1*, *2*). The estimates of the size of the earthquake from seismic data are highly sensitive to the method and frequency band used in the analysis and range from the initial Harvard CMT estimate of scalar seismic moment $M_0 = 4.0 \times 10^{22}$ Nm (M_w 9.0) to as much as three times that amount, as inferred from very-long-period data (>500 s) (*3*). Static surface offsets are caused by the elastic deformation of Earth in response to the earthquake. Geodetic measurements of these motions can be used to derive kinematic rupture models and calculate the size of the event, independent of the seismic energy released by the earthquake.

Here we use data from 41 continuously operating Global Positioning System (GPS) stations to calculate coseismic surface displacements throughout Southeast Asia (*4*). All but five of the stations are located at distances >1000 km from the earthquake epicenter (Fig. 1). We combined our own solutions with daily solutions of global International GNSS Service (IGS) stations (*5*). The GPS data were processed with the GAMIT/GLOBK software package to produce time series of station coordinates in the ITRF-2000 reference frame spanning at least 20 days before and after the earthquake (supporting online text and fig. S1). We estimated offsets at the time of the earthquake by differencing the mean positions in the 5 days before and after the earthquake, respectively. Data from the first 5 hours after the earthquake are not included in that day's solution. We used only the horizontal components in our analysis. We also used estimated offsets from campaign GPS measurements on the Andaman and Nicobar Islands (*6*). The GPS data show that there was a coherent surface motion roughly directed toward the earthquake rupture at distances up to 4500 km from the epicenter (Fig. 1 and table S1).

The standard approach of modeling the surface motions from an earthquake with an elastic half-space approximation of Earth (*7*) is inappropriate for an event of the magnitude and dimensions of the Sumatra earthquake. We model the event using PREM, a spherically layered elastic structure of the Earth determined from inversion of Earth's free-oscillation spectra (*8*, *9*). Static deformation in a spherical geometry is evaluated with the method described in (*10*, *11*). Forward model comparisons of the Sumatra earthquake show that surface motions calculated with a homogeneous spherical model greatly exceed surface motions of the layered spherical model at large distances (fig. S2).

We define the geometry of the earthquake rupture based on constraints provided by the distribution of aftershocks and independent seismic source studies (*1*). We subdivided the model geometry into three principal along-strike segments aligned with the strike of the megathrust from Sumatra to the northern Andaman Islands (table S2). The magnitudes of the far-field displacements are highly sensitive to fault dip (fig. S4), and we thus subdivided each segment in our model into two subsegments to simulate the dip increase with depth. This geometry is consistent with seismic constraints of depths to the top of the slab (*12*) and the ~30° nodal-plane dips of a large cluster of aftershocks at ~5°N and depths of 45 to 50 km (Fig. 2). Seismic source studies suggest that the rake of the rupture became more oblique toward the north (*2*). Little strike-slip motion on the southern segment is evident in the focal mechanism solutions of the aftershocks, but strike-slip motion appears likely on the Andaman and Nicobar segments (segments 1 and 2 in Fig. 2). The first-order models that we consider therefore involve uniform dip-slip and strike-slip components on the Andaman and Nicobar segments and uniform dip slip on the southern segment.

If we solve for the optimal uniform slip values on each rupture segment (Model M1 in Table 1), the slip averages more than 5 m on all segments. The displacement field predicted by this model (Fig. 1A) fits the GPS data set well at all distance ranges. A second case (Model M2), which does not allow for slip on the Andaman segment, results in a significantly worse fit (*13*) (Table 1). The predicted displacement field of Model M2 (Fig. 1B) fails particularly to predict the coseismic offsets of Indian sites, which moved up to 25 mm eastward. This confirms that the Andaman segment participated in the Sumatra-Andaman earthquake sequence and slipped by several meters predominantly as dip slip, but with a minor, right-lateral strike-slip component.

A variation of Model M1 in which the deeper subsegment of segment 3 is neglected leads to a significantly worse fit (reduced χ^2 = 1.63 versus 1.36 for Model M1). The sensitivity to fault dip around the southern part of the rupture arises from the large dependence of displacement azimuth on dip at Sumatran sites south of the equator (fig. S4). This result indicates that the deeper portion of the megathrust in the southernmost part of the rupture participated with several meters of slip, consistent with the occurrence of deeper aftershocks there (Fig. 2). If we restrict slip on the northern segments 1 and 2 to their shallowly dipping portions, the data set is fit nearly as well as that involving slip on the wider faults,

[1]Wadia Institute of Himalayan Geology, Dehra Dun, 248001, India. [2]U.S. Geological Survey, Menlo Park, CA 94025, USA. [3]Department of Earth and Planetary Science and Berkeley Seismological Laboratory, University of California, Berkeley, CA 94720, USA.

*To whom correspondence should be addressed. E-mail: burgmann@seismo.berkeley.edu

and estimated slip values nearly double (Model M3 in Table 1 and Fig. 1C).

These kinematic models may be compared with available horizontal movements determined from campaign GPS measurements of the Andaman and Nicobar Islands (*6*) (Fig. 2). Model M3 generally matches well the measured offsets, whereas Model M1 predicts offsets that are too small and predicts the incorrect sense of uplift at some of these sites. These comparisons indicate that most of the coseismic slip was shallow (less than ~30-km depth) in these regions. However, the actual slip distribution is expected to be more complex than predicted by our simple uniform slip models, consistent with substantial heterogeneity in the observed near-field uplift and subsidence patterns along the island chains (*14*).

The scalar seismic moment of the earthquake sequence calculated with Model M1 is $M_0 = 5.67 \times 10^{22}$ Nm, corresponding to a moment magnitude of $M_w = 9.14$. This value is 40% larger than the seismic moment determined in the Harvard CMT solution using long-period body waves and surface waves up to 300-s period. It is about one-half of that determined by (*3*) using free oscillations up to 1-hour period, which corresponds to $M_w = 9.30$. We note that source excitation of very-long-period fundamental spheroidal modes (*15*) is primarily through the moment tensor components M_{rr} and $(M_{tt} + M_{pp})$, which are proportional to $slip \times \sin(\lambda) \times \sin(2\delta)$, where λ is fault rake and δ is dip, and subscripts r, t, and p refer to the local vectors $\hat{r}$, $\hat{\theta}$, and $\hat{\phi}$ in a spherical coordinate system. With moderate dips of $\delta = 35°$ used here on the deeper portions of the various segments, the contribution to the free-oscillation excitation is equivalent to that produced by a 15°-dipping fault with twice the slip. An increase in seismic moment will therefore result if slip is constrained to be on the shallowly dipping portions of the fault segments. This prediction is verified by Model M3, which is identical to Model M1 except that slip on segments 1 and 2 is restricted to their shallowly dipping portions and has an increased $M_w = 9.17$. The best-fitting point source constrained to the CMT source depth of 28.4 km and dip of 8° [i.e., the source depth and dip assumed by (*3*)] results in $M_w = 9.37$ (Model P in Table 1) and a scalar moment M_0 that is 27% greater than that estimated by (*3*). The sensitivity of the scalar moment to fault dip is directly illustrated in Fig. 3A, where M_0 estimated from inversion for the best-fitting point source exhibits a $\sim(\sin 2\delta)^{-1}$ dependence, whereas the estimated moment tensor component M_{rr} varies little with changing dip. Thus, once the steeper average dip of the Sumatra rupture is taken into consideration, the estimated moment magnitude does not exceed $M_w = 9.2$.

The static displacement field measures earthquake size at periods far greater than the ~1-hour period measured by Earth's free oscillations (*3*). A useful measure of the earthquake size is the combination of moment tensor components M_{rr} and $(M_{tt} + M_{pp})$, which dominate the excitation of both the

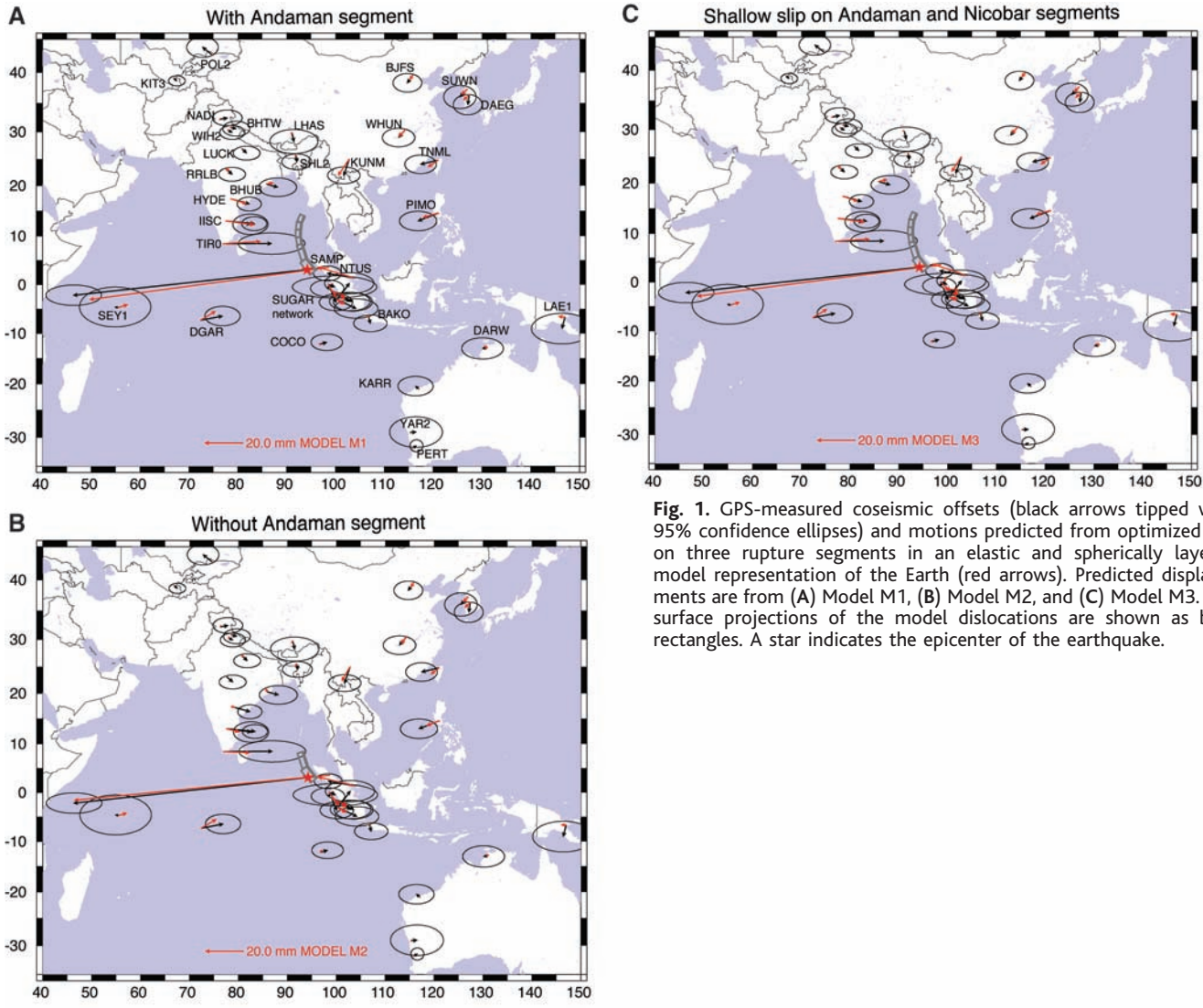

Fig. 1. GPS-measured coseismic offsets (black arrows tipped with 95% confidence ellipses) and motions predicted from optimized slip on three rupture segments in an elastic and spherically layered model representation of the Earth (red arrows). Predicted displacements are from (**A**) Model M1, (**B**) Model M2, and (**C**) Model M3. The surface projections of the model dislocations are shown as bold rectangles. A star indicates the epicenter of the earthquake.

low-degree fundamental spheroidal modes and the static displacements. Because $M_{rr} = -(M_{tt} + M_{pp})$ for a shear dislocation, we consider the single measure M_{rr}, which has the advantage of being nearly geometry independent (Fig. 3A). The model of (*3*) corresponds to $M_{rr} = 2.59 \times 10^{22}$ Nm. Our finite source models yield $M_{rr} = 3.26 \times 10^{22}$ to 3.61×10^{22} Nm (Table 1). Figure 3B demonstrates a systematic increase in M_{rr} with period, including the CMT solution involving periods <300 s and the seismic slip inversion of (*1*) at periods up to 2000 s. This trend, first noted by (*3*), implies that about 25 to 35% of the total seismic moment release occurred beyond the ~1-hour time scale that is directly detectable with seismic waves.

The precise time of cessation of substantial moment release is uncertain. The GPS time series (fig. S1) qualitatively suggest an upper bound of 1 day. If most or all of the post-1-hour slip were confined to the Andaman segment, then the evolution of aftershocks may provide guidance. Moderate-sized earthquakes on the Andaman segment may have occurred on localized asperities simultaneously with predominantly aseismic slip. The rate of moderate earthquakes on the Andaman segment (Fig. 3B) suggests that a large part of the slip occurred between 40 min after the mainshock, coinciding approximately with the initiation of coseismic subsidence of Port Blair (*14*), and 2.5 hours after the mainshock.

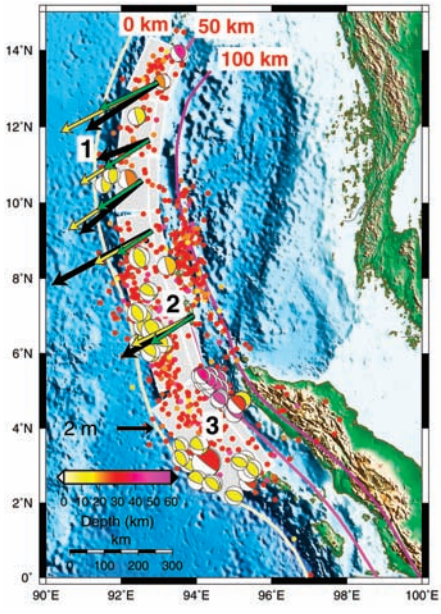

Fig. 2. Three-segment fault geometry of the Sumatra-Andaman Islands earthquake. Superimposed are the hypocenters of $M > 4$ earthquakes occurring from 26 December 2004 to 5 January 2005 from the National Earthquake Information Center (NEIC) catalog, the subset of CMT aftershock focal mechanisms with reverse slip (plunge of tension axis > 45°), and the 0-, 50-, and 100-km isocontours of the slab-top depth from (*12*). Fault geometry parameters are in table S2. Also shown are horizontal GPS offsets (solid black arrows) from the Andaman and Nicobar Islands from (*6*) compared with the predictions of Models M1 (green) and M3 (yellow).

References and Notes

1. T. Lay *et al.*, *Science* **308**, 1127 (2005).
2. C. J. Ammon *et al.*, *Science* **308**, 1133 (2005).
3. S. Stein, E. Okal, *Nature* **434**, 581 (2005).
4. The GPS data are from stations belonging to the IGS global network, the BAKOSURTANAL Indonesian network, the Sumatran GPS Array operated by the Tectonic Observatory at Caltech and the Indonesian Institute of Science (LIPI), and the Indian "National Program on GPS" Network of the Department of Science and Technology made available by the Survey of India GPS Data Centre.
5. We use daily solutions of global GPS stations processed and archived at the Scripps Orbital and Permanent Array Center (http://sopac.ucsd.edu). Eighteen IGS stations located >5000 km from the rupture are used in the ITRF-2000 reference frame realization. Our regional solution includes 25 stations, 9 of which are in common with the SOPAC solution (table S1).
6. C. P. Rajendran, A. Earnest, K. Rajendran, R. Bilham, J. T. Freymueller, in preparation.
7. Y. Okada, *Bull. Seismol. Soc. Am.* **75**, 1135 (1985).
8. A. M. Dziewonski, D. L. Anderson, *Phys. Earth Planet. Int.* **25**, 297 (1981).
9. The PREM model contains large increases in rigidity at major discontinuities at depths of 25 km (Mohorovocic discontinuity), 220 km (base of asthenosphere), 400 km, and 670 km (upper mantle–lower mantle boundary), followed by a decrease to zero rigidity at 2891 km (core-mantle boundary). Our modeling includes the fluid outer core but not the solid inner core.
10. F. F. Pollitz, *Geophys. J. Int.* **125**, 1 (1996).
11. A spherical harmonic expansion from l=1 to l=1500 is used to represent the spherical displacement fields. The l=1 component is found to be very important for correctly synthesizing far-field displacements. For typical Sumatra slip models, the predicted displacement at the farthest (Korean) sites amounts to several mm and arises almost entirely from the l=1 component of the displacement field.

Table 1. Fit of Sumatra slip models to far-field GPS. u_i and λ_i denote, respectively, slip and rake on fault *i*. We hold fixed $\lambda_3 = 90°$. Inversions are subjected to the constraint $90° = \lambda_3 \leq \lambda_2 \leq \lambda_1$. Variable rake on fault-1 subsegments is described in table S2.

Model	u_1 (m)	λ_1 (°)	u_2 (m)	λ_2 (°)	u_3 (m)	χ^{2*}	M_0 (10^{22} Nm)	M_{rr} (10^{22} Nm)	M_w
M1	5.3 ± 0.8	104 ± 5	9.2 ± 1.6	104 ± 7	6.0 ± 0.3	1.36	5.93	3.61	9.15
M2	0†	0†	14.4 ± 1.4	105 ± 7	5.8 ± 0.3	1.70	4.85	3.26	9.09
M3‡	10.5 ± 1.6	105 ± 5	14.1 ± 2.2	105 ± 8	6.6 ± 0.3	1.42	6.42	3.26	9.17
P‖						1.52	12.66	3.43	9.37

*Reduced χ^2, equal to the full χ^2 divided by $N - n$, where $N = 82$ is the number of data constraints and n is the number of independent parameters ($n = 5$ for Models M1 and M3, $n = 3$ for Model M2, $n = 5$ for Model P). †Value fixed in inversion. ‡Uniform slip on segments 1 and 2 is restricted to their respective shallow portions, i.e., only from 0- to 30-km depth. ‖Best-fitting point source constrained to CMT depth of 28.4 km and dip of 8°. Point source location and geometry: 8.0°N, 93.3°E, strike = 340°, rake = 102°. $\chi^2 = 1.52$ excluding SAMP, $\chi^2 = 6.19$ with SAMP.

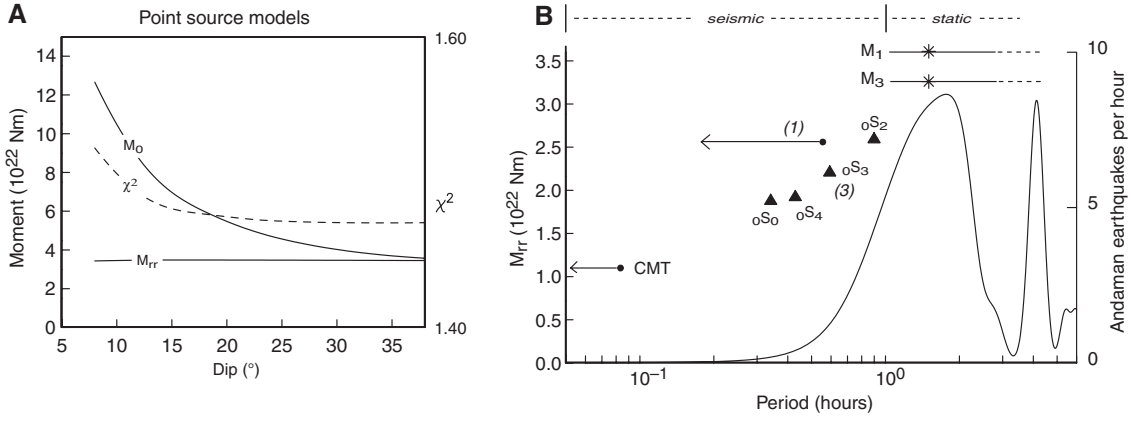

Fig. 3. (**A**) Scalar seismic moment M_0 and moment tensor component M_{rr} derived from inversion of GPS data set for best-fitting point source subject to fixed position at 8.0°N, 93.3°E, strike 340°, and CMT source depth of 28.4 km. Right-hand axis displays the corresponding reduced χ^2 excluding SAMP. (All static point source models yield a poor fit to SAMP.) (**B**) Moment tensor component M_{rr} derived from the CMT solution (periods <300 s), the seismic slip inversion of (*1*) (periods <2000 s), and free oscillations (*3*) compared with that of Models M1 and M3 derived from the far-field static offset. An average rake of 110° and average fault dip of 13.5° were assumed to convert scalar seismic moment of 6.0×10^{22} Nm estimated in (*1*) to the corresponding M_{rr}. Black curve is the rate of $M \geq 5$ earthquakes (from NEIC catalog) that occurred on the Andaman segment as a function of time after the mainshock, smoothed using a Gaussian scaling time of 0.25 hours. Shallow aftershocks in the back-arc region (8°N to 10°N and east of ~93.5°E) (Fig. 2) are excluded.

12. O. Gudmundsson, M. Sambridge, *J. Geophys. Res.* **103**, 7121 (1998).
13. A statistical F-test shows that the improvement in data fit with respect to Model M2 by including the additional two parameters of the Andaman segment is significant at 99.93% confidence (Model M1) or 99.76% confidence (Model M3).
14. R. G. Bilham, E. R. Engdahl, N. Feldl, S. P. Satyabala, *Seismol. Res. Lett.*, in press.
15. F. Gilbert, A. M. Dziewonski, *Philos. Trans. R. Soc. London Ser. A* **278**, 187 (1975).
16. We thank C. P. Rajendran and R. Bilham for providing results before publication. GPS data processing was carried out under a Department of Science and Technology, Government of India–sponsored project (to P.B.).

Supporting Online Material
www.sciencemag.org/cgi/content/full/1113746/DC1

SOM Text
Figs. S1 to S4
Tables S1 and S2
References and Notes

18 April 2005; accepted 10 May 2005
Published online 19 May 2005;
10.1126/science.1113746
Include this information when citing this paper.

Dilution of the Northern North Atlantic Ocean in Recent Decades

Ruth Curry[1]* and Cecilie Mauritzen[2]

Declining salinities signify that large amounts of fresh water have been added to the northern North Atlantic Ocean since the mid-1960s. We estimate that the Nordic Seas and Subpolar Basins were diluted by an extra 19,000 ± 5000 cubic kilometers of freshwater input between 1965 and 1995. Fully half of that additional fresh water—about 10,000 cubic kilometers—infiltrated the system in the late 1960s at an approximate rate of 2000 cubic kilometers per year. Patterns of freshwater accumulation observed in the Nordic Seas suggest a century time scale to reach freshening thresholds critical to that portion of the Atlantic meridional overturning circulation.

The salinities of water masses originating in the high-latitude North Atlantic Ocean have been cascading downward since the early 1970s (*1*–*4*). This region has climatic importance because the Nordic Seas and the Labrador and Irminger basins are sites where cold, dense waters are formed—an integral component of what is often termed the meridional overturning circulation (MOC). The Atlantic MOC involves a northward flow of warm surface waters in exchange for a southward flow of cold, dense waters in the deep ocean along the pathways shown in Fig. 1. This component of circulation transports heat northward and thus contributes to moderating the cold-season climate at high northern latitudes. Excessive amounts of fresh water could alter the ocean density contrasts that drive the northernmost extension of the Atlantic MOC, diminish its northward heat transport, and substantially cool some regions of the North Atlantic (*5*–*10*). The MOC's sensitivity to greenhouse warming remains a subject of much scientific debate (*10*). The observed freshening does not yet appear to have substantially altered the MOC and its northward heat transport (*11*, *12*). But uncertainties regarding the rates of future greenhouse warming and glacial melting limit the predictability of their impact on ocean circulation (*8*, *10*).

What has been missing from the evolving picture thus far is an explicit quantification of how much additional fresh water it took to cause the observed salinity changes, how fast it entered the sub-Arctic ocean circulation, and where that fresh water had been stored. All three factors are important for assessing the present and future impacts of freshening on the Atlantic MOC, and provide the types of information that facilitate climate model validation studies. To address these issues, we reconstructed the history of volumetric changes in ocean temperature, salinity, and density in the Nordic Seas and Subpolar Basins and estimated the magnitude of freshwater storage and net volume flux anomalies required to account for the observed dilution over the past 50 years. We then examined the degree to which density has responded to this freshening, as a means of gaining perspective on its seemingly negligible MOC impact. Finally, we used this perspective to estimate how much additional fresh water might be required to equalize the density contrast that contributes to the exchange of mass and heat between the Nordic Seas and the subpolar North Atlantic.

Extensive amounts of hydrographic data have been collected in the seas between Labrador and northern Europe in the past 50 years. We used these data to construct well-constrained, three-dimensional representations of ocean properties for successive 5-year time frames spanning the years 1953 to 2002 (*13*). Because salinity is approximately conserved in the ocean, salinity anomaly fields can be used to quantify the volume of additional fresh water that had to be added or removed to account for salinity changes accumulated through the entire water column (*13*). Mapping this quantity, layer by layer, time frame by time frame, throughout the domain describes the evolution of freshwater storage in space and time. Integrating it over a geographic area provides a history of the volumetric freshwater storage anomaly in cubic kilometers, and differencing this storage anomaly in consecutive time frames implies a rate of change—the net freshwater flux anomaly—in sverdrups (1 Sv = 10^6 m^3 s^{-1}).

Time series of freshwater storage anomaly and net flux anomaly for the Nordic Seas and Subpolar Basins were considered separately and as a whole (Fig. 2) (table S1). From the earliest part of the record through the mid-1960s, salinities increased in the upper 2000 m of all the Subpolar Basins. Its volumetric expression was a net loss in subpolar freshwater storage of ~5000 km^3 between 1955 and 1965. By contrast, the net change in the Nordic Seas was comparatively small at that time. Between 1965 and 1990, however, both the Nordic Seas and Subpolar Basins became increasingly freshened. Net freshwater storage increased by ~19,000 km^3, of which ~4000 km^3 spread into the Nordic Seas and ~15,000 km^3 accumulated in the Subpolar Basins. A recovery from the early 1990s peak of freshwater storage in the Subpolar Basins occurred in the mid-1990s, but our volumetric analysis falters for the last time frame (1998 to 2002) because of inadequate data coverage (*14*). For the Nordic Seas, an approximate balance between import and export of fresh and saline waters resulted in little net volumetric change in the late 1990s.

The most striking event of the time series occurred in the early 1970s. During the late 1960s, a large pulse of fresh water entered the Nordic Seas through Fram Strait and rapidly moved southward along the western boundary in the East Greenland Current. This event has been labeled the Great Salinity Anomaly (GSA) (*15*), and we can here confirm that the name is appropriate, for it contributed an extra ~10,000 km^3 of fresh water to the sub-Arctic seas in the late 1960s and early 1970s, implying a net flux anomaly of ~0.07 Sv during a 5-year period. The GSA was previously thought to be equivalent to ~2000 km^3 of excess fresh water (*15*) and has been attributed to several years of anomalously large sea ice export from the Arctic (*16*, *17*). The Arctic freshwater budget includes inflows from the Pacific (~1600 km^3 year^{-1}) and rivers (~3500 km^3 year^{-1}) that are mainly balanced by annual exports of fresh water and sea ice through Fram Strait and the Canadian

[1]Woods Hole Oceanographic Institution (WHOI), Woods Hole, MA 02543, USA. [2]Norwegian Meteorological Institute, 0313 Oslo, Norway.

*To whom correspondence should be addressed. E-mail: rcurry@whoi.edu

The Size and Duration of the Sumatra-Andaman Earthquake from Far-Field Static Offsets

Supporting Online Material

P. Banerjee, (1), F.F. Pollitz, (2), and R. Bürgmann (3)

(1) Wadia Institute of Himalayan Geology, Dehra Dun, 248001, India
(2) U.S. Geological Survey, Menlo Park, CA 94025, USA
(3) Department of Earth and Planetary Science and Berkeley Seismological Laboratory, University of California, Berkeley, CA 94720, USA

Supporting online text

The Sumatra-Andaman earthquake produced observable static offsets at distances greater than 4500 km from the rupture, and it requires a spherical geometry to understand its global impact. Here we provide additional information on the GPS results and explore how predicted static deformation fields interact with Earth's elastic layering and sphericity.

The GPS data were processed using the GAMIT/GLOBK software package (S*1, S2*) to produce time series of station coordinates in the ITRF-2000 reference frame spanning at least 20 days before and after the earthquake. Fig. S1 shows GPS-position time series spanning the earthquake from 5 representative stations (IISC, KUNM, TNML, DGAR and SAMP in Fig. 1). The pre-earthquake time series illustrate background short-term and longer-term fluctuations in the data. Offsets are estimated by differencing 5-day averages from before and after the earthquake. The uncertainty estimates of the offsets are derived from the formal GPS solution errors. Fig. S1F shows the distribution of the 18 global IGS GPS stations that were used to implement the ITRF-2000 reference frame in the GPS analysis. Stations used to define the reference frame are located at distances > 4500 km from the earthquake rupture.

Fig. S2 illustrates the effect of Earth's layering using the PREM model to specify depth-dependent elastic parameters. Because of the increase in rigidity with depth, predicted displacements from thrust faulting on a realistically-layered sphere fall off with distance much more rapidly than those calculated on a homogeneous sphere.

The comparison between homogeneous-sphere and half-space approaches in Fig. S3 illustrates how Earth's sphericity affects the horizontal displacement field produced by thrust

faulting. The amplitude of the displacement field is profoundly affected by the sphericity, especially at great distance (i.e., NE Asia) where displacements on the sphere are several times larger than those produced on a homogeneous half-space. The homogeneous spherical and half-space treatments were previously compared in *(S3)*, where agreement was found generally within a few percent out to about 5 geocentric degrees from the source, with deeper sources producing a greater interaction with sphericity. Additional synthetic tests show that divergence between the two cases grows quickly beyond about 10 geocentric degrees.

Fig. S4 illustrates the sensitivity of horizontal displacements to fault dip. Uniform slip values are specified on the set of shallow-dipping sub-segments (those with dip ≤ 18°. in Table S2) and the set of steeply-dipping sub-segments (those with dip = 35°) such that the seismic moment on each set is identical. The senses of motion produced in the two cases are parallel, but the motions generated by slip on the more steeply-dipping faults is about twice as great. This indicates that there is a substantial tradeoff between fault dip and scalar seismic moment; i.e., estimates of seismic moment derived from fitting a given set of displacements are expected to be larger when relatively shallowly-dipping planes are specified.

Supporting Figures

Fig. S1. Time series of E, N and vertical components of GPS site positions for 4 representative stations starting > 100 days before and ending 20 days after the December 26, 2004 earthquake. The time of the earthquake is indicated by a vertical line. Coseismic offsets were estimated from mean positions during five days before and after the event, respectively. Data from the first 5 hours following the earthquake are not included in that day's solution. (a) IISC – Bangalore, India, (b) KUNM – Kunming, China, (c) TNML – Hsinchu, Taiwan, (d) DGAR – Diego Garcia Island, (e) SAMP - Sampali-Medan, Indonesia, (f) Distribution of global GPS stations used to establish the ITRF-2000 reference frame in the GPS analysis (filled triangles) shown together with the calculated coseismic offsets used in this study (arrows with 95% confidence ellipses). Highlighted station names and bold arrows indicate the sites whose time series are shown in (a)-(e).

Fig. S2. Comparison of forward models calculated using the layered, spherical Earth model used in this study (PREM) and those predicted using a homogeneous sphere with Poisson's ratio of 0.25. Both models have dip slip of 7 m assigned to all fault segments. Note that the homogeneous sphere model predicts similar motions to the layered model within about one rupture length of the model, while it produces much smaller offsets at distances greater than ~1500 km.

Fig. S3. Comparison of forward models calculated using a homogeneous sphere with Poisson's ratio of 0.25 and those predicted with a homogeneous half-space. Both models have dip slip of 7 m assigned to all fault segments.

Fig. S4. Dependence of predicted site motions on fault dip. Black arrows show the static displacement field calculated with 15 m slip assigned to the shallowly-dipping portions of the fault segments. Gray arrows show the static displacement field calculated with 8.167 m slip assigned to the shallowly-dipping portions of the fault segments. The slip values are chosen such that the scalar seismic moment values specified on the set of shallowly-dipping planes (which are about 100-km wide) and the set of steeply-dipping planes (which are about 35-km wide) are identical and equal 4.71×10^{22} N m.

A

IISC North Offset 1449509.543 m

wmean(mm)= 9543.70 ± 0.23 nrms= 1.21 wrms= 3.1 mm # 123

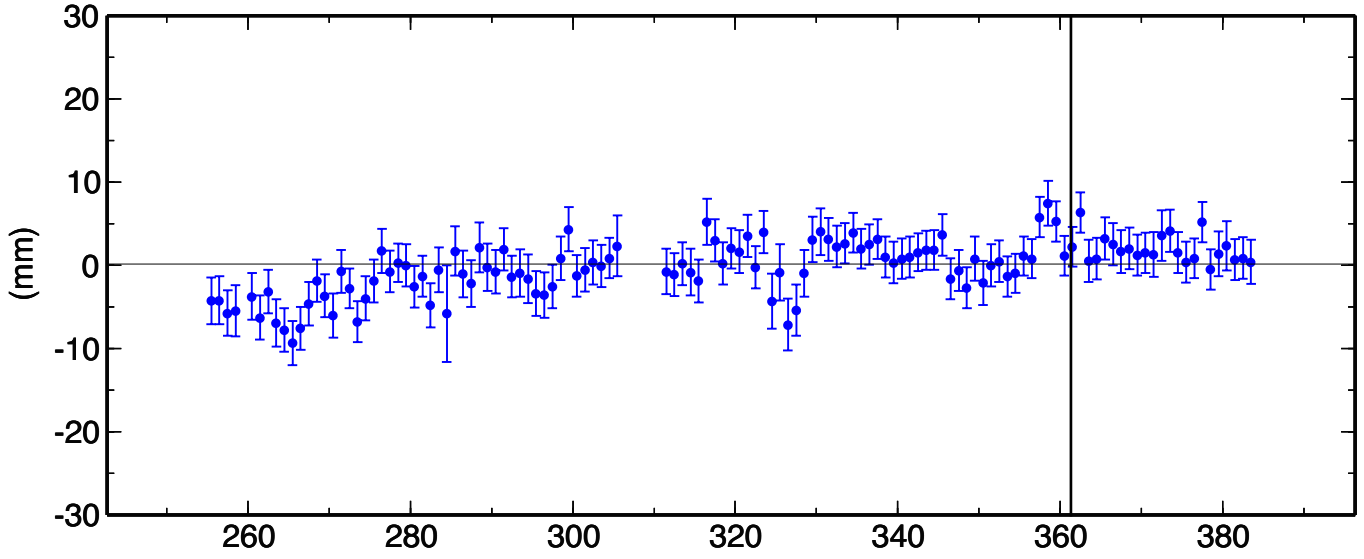

IISC East Offset 8413090.573 m

wmean(mm)= 571.74 ± 0.40 nrms= 2.37 wrms= 10.5 mm # 122

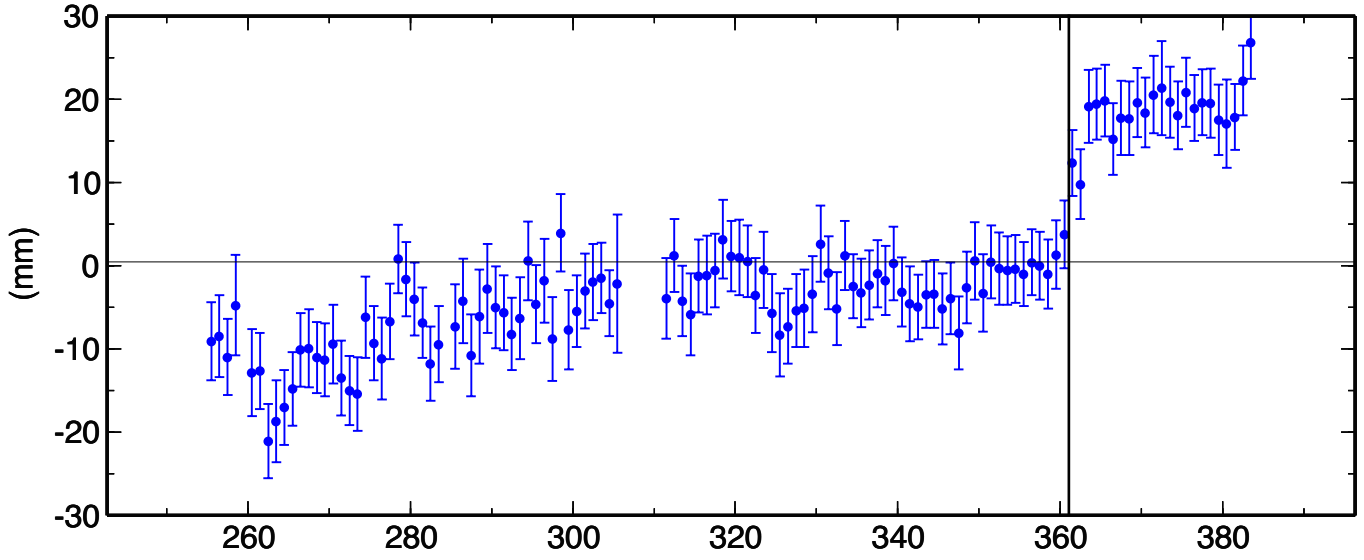

IISC Up Offset 843.704 m

wmean(mm)= 3704.69 ± 0.72 nrms= 0.81 wrms= 6.5 mm # 123

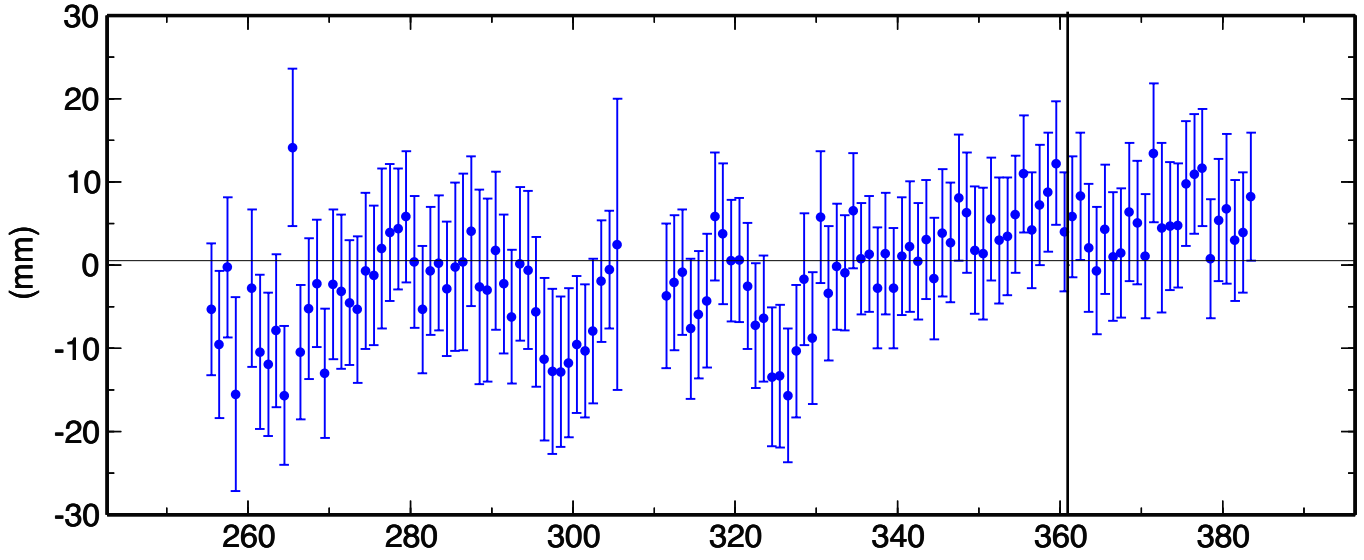

B

KUNM North Offset 2786275.506 m

wmean(mm)= 5507.53 ± 0.25 nrms= 1.55 wrms= 4.4 mm # 126

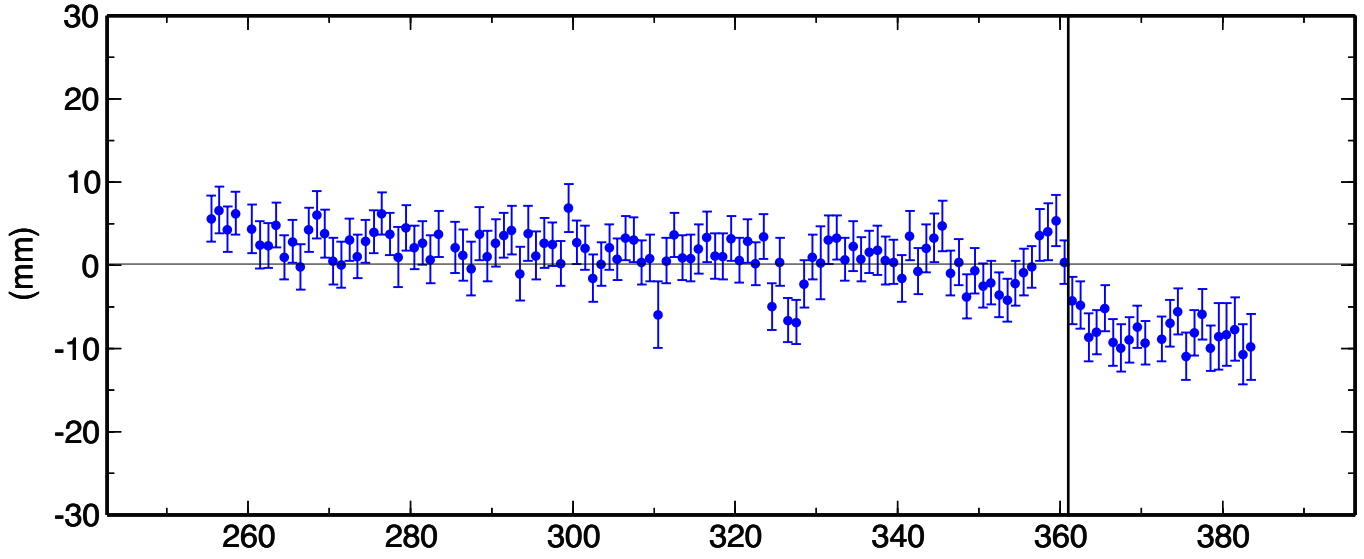

KUNM East Offset 10368693.187 m

wmean(mm)= 3193.25 ± 0.52 nrms= 0.80 wrms= 4.6 mm # 126

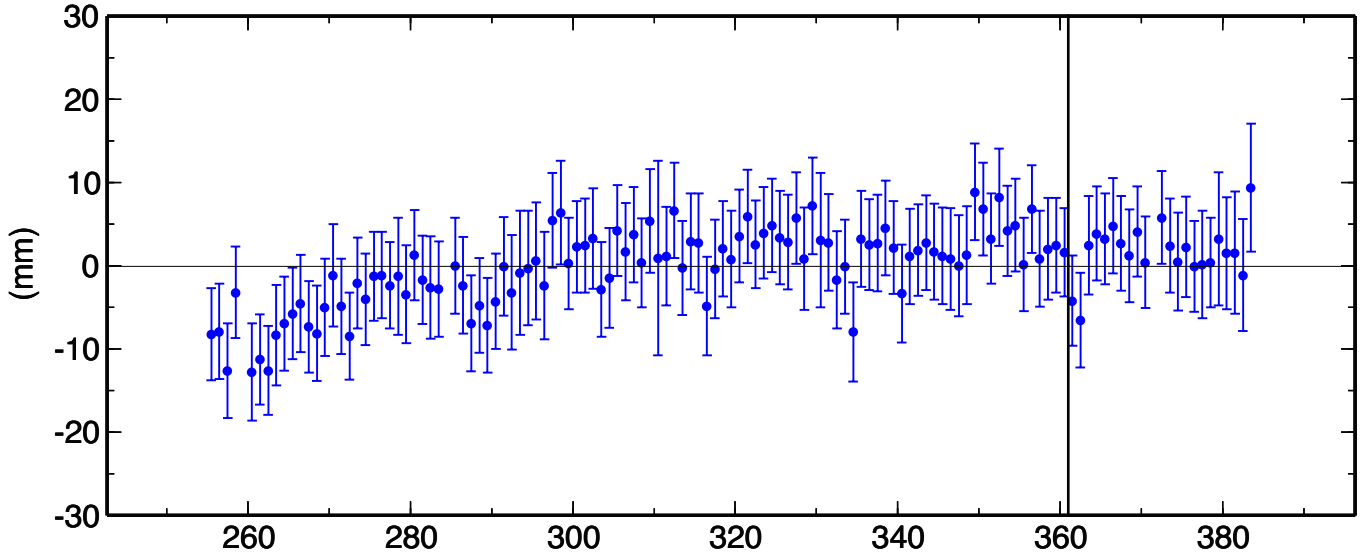

KUNM Up Offset 1986.190 m

wmean(mm)= 6193.97 ± 1.08 nrms= 0.66 wrms= 8.1 mm # 128

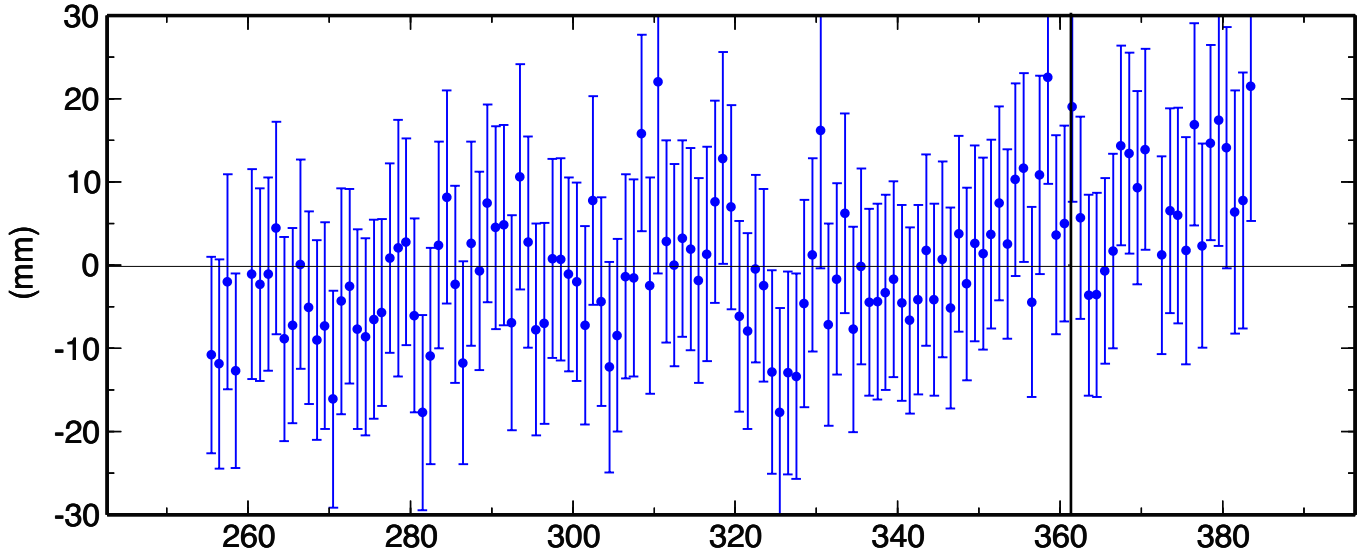

TNML North Offset 2760495.669 m

wmean(mm)= 5668.01 ± 0.28 nrms= 1.05 wrms= 3.1 mm # 115

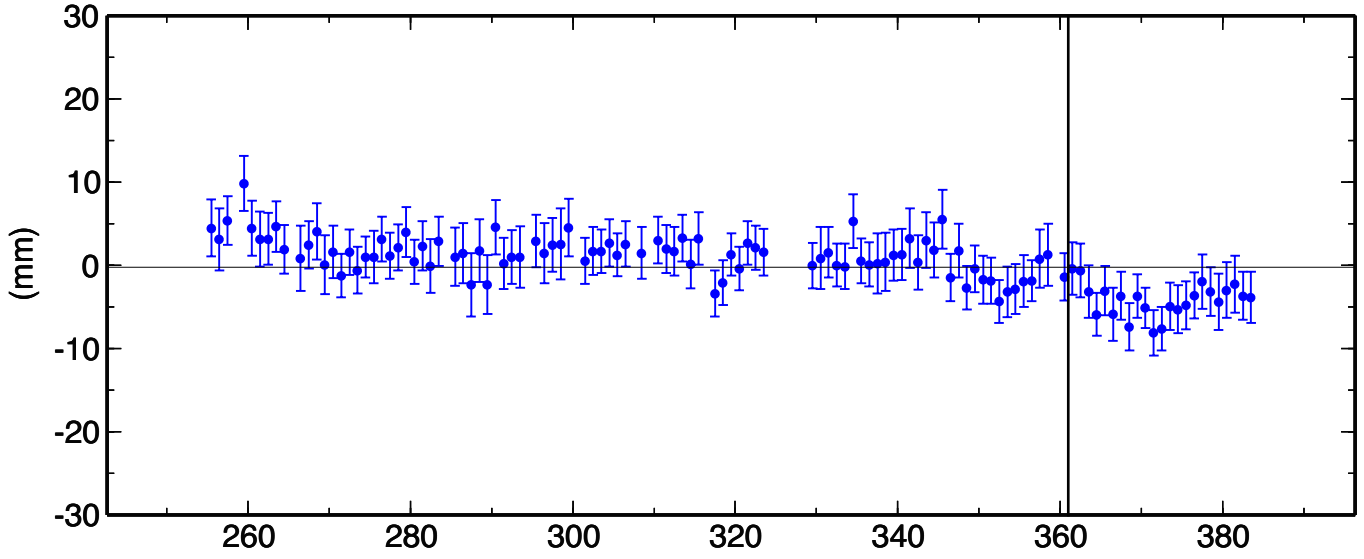

TNML East Offset 12226429.739 m

wmean(mm)= 9741.40 ± 0.48 nrms= 1.01 wrms= 5.2 mm # 115

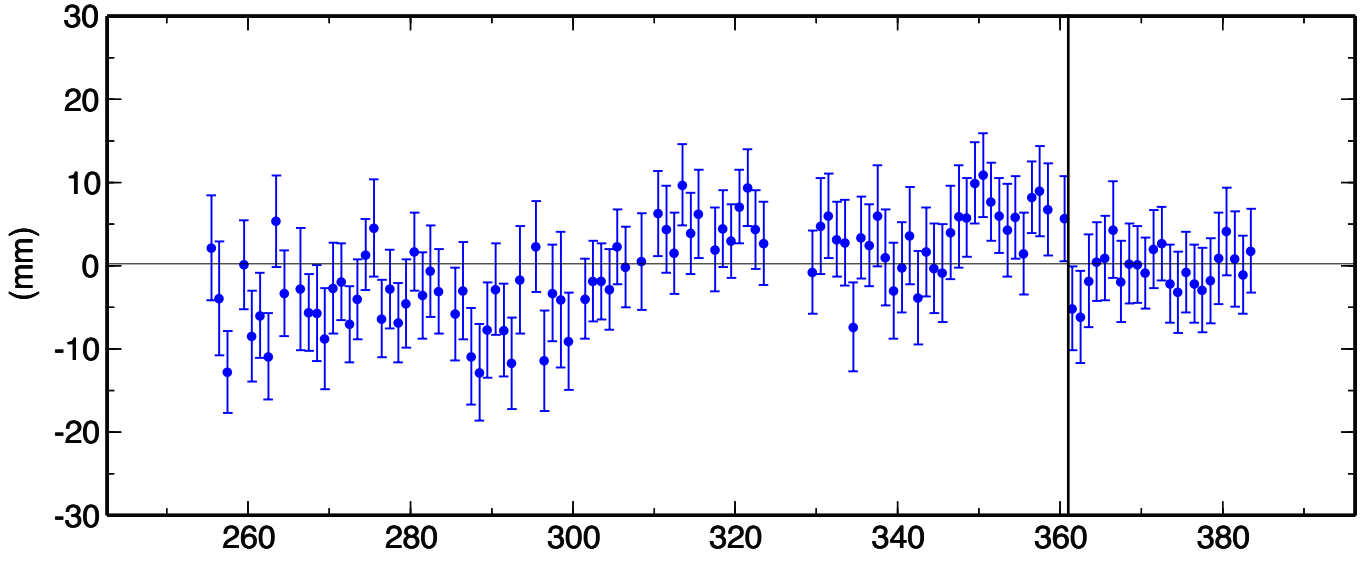

TNML Up Offset 75.853 m

wmean(mm)= 5854.13 ± 0.79 nrms= 0.61 wrms= 5.3 mm # 116

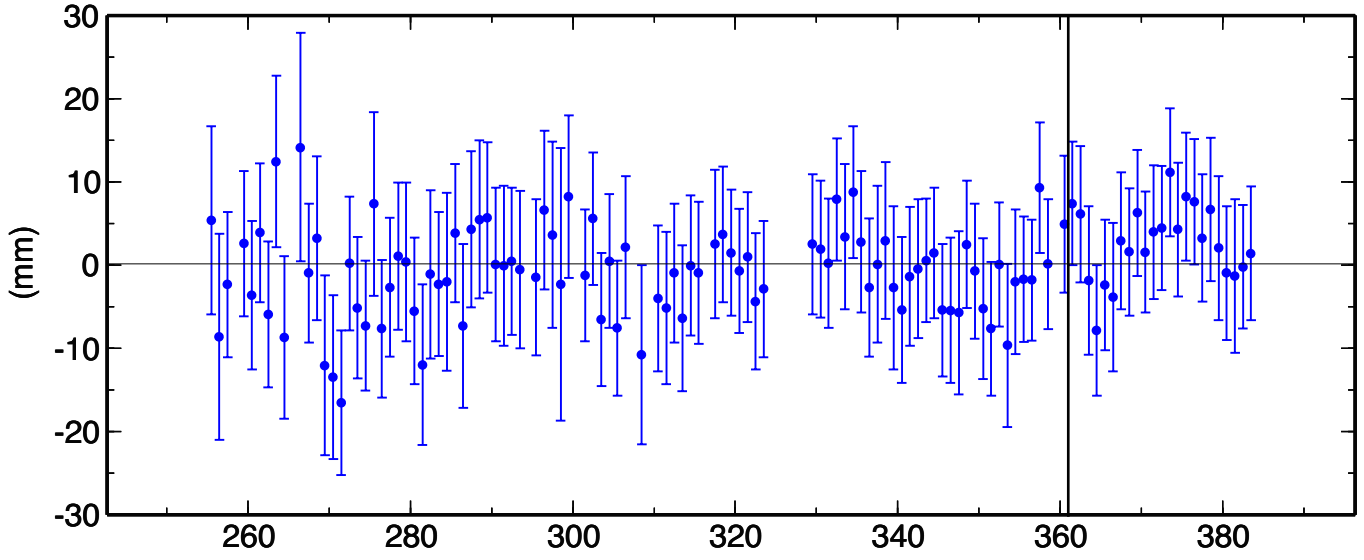

D

DGAR North Offset -809257.691 m

wmean(mm)= -7693.83 ± 0.30 nrms= 1.64 wrms= 5.6 mm # 129

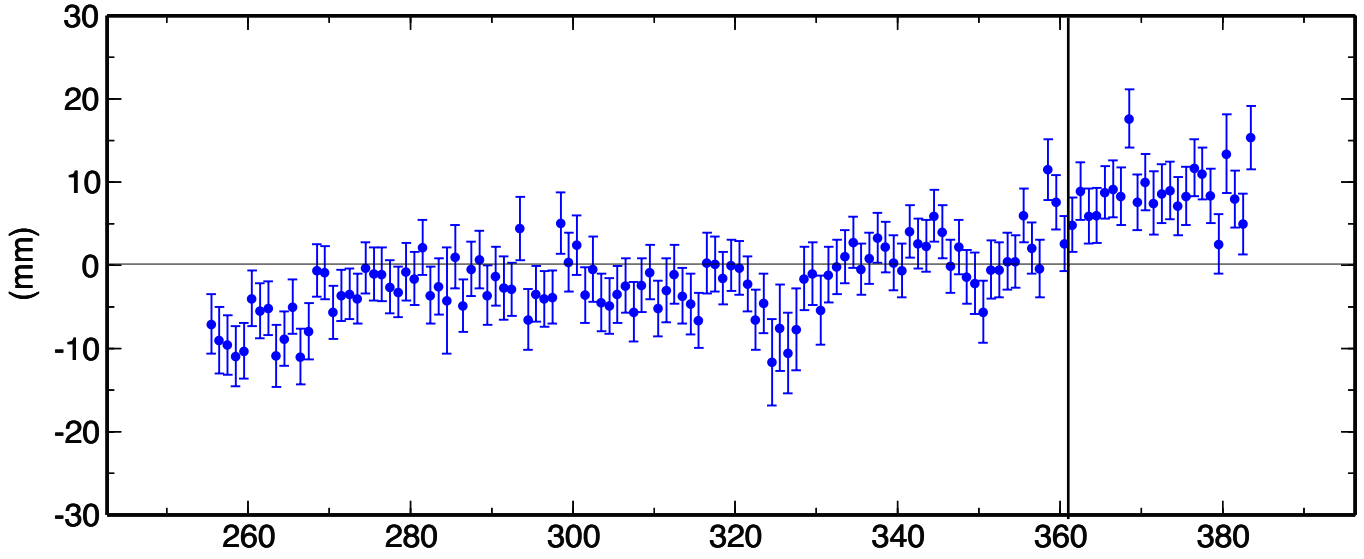

DGAR East Offset 7991434.290 m

wmean(mm)= 4294.89 ± 0.51 nrms= 1.35 wrms= 7.9 mm # 129

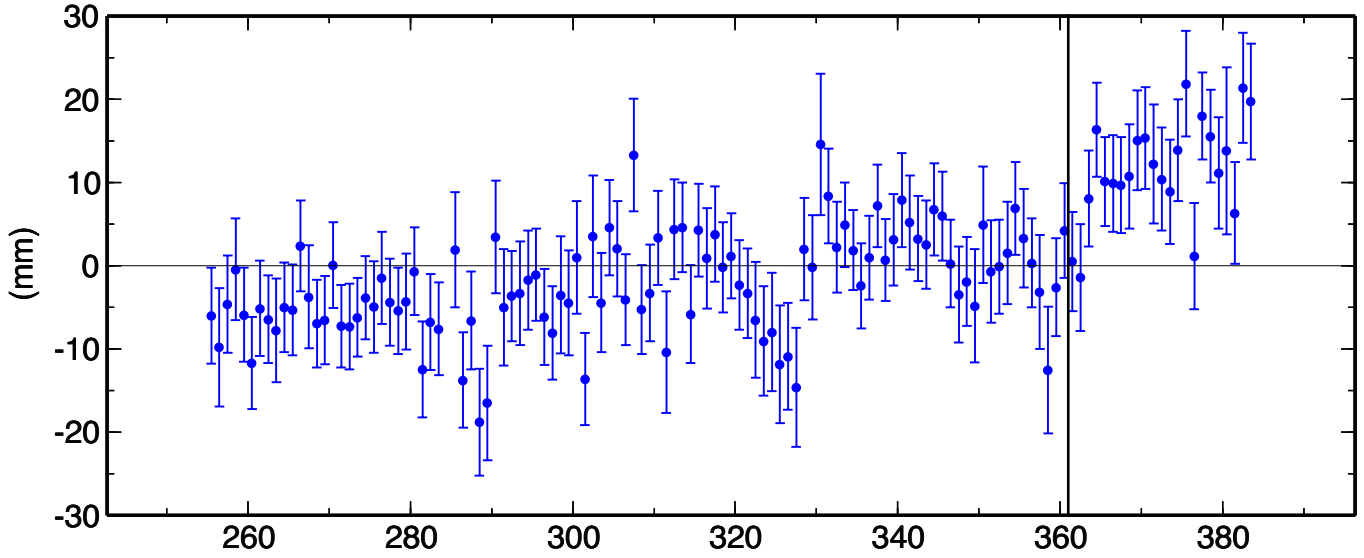

DGAR Up Offset -64.920 m

wmean(mm)= -4924.27 ± 0.82 nrms= 1.03 wrms= 9.6 mm # 129

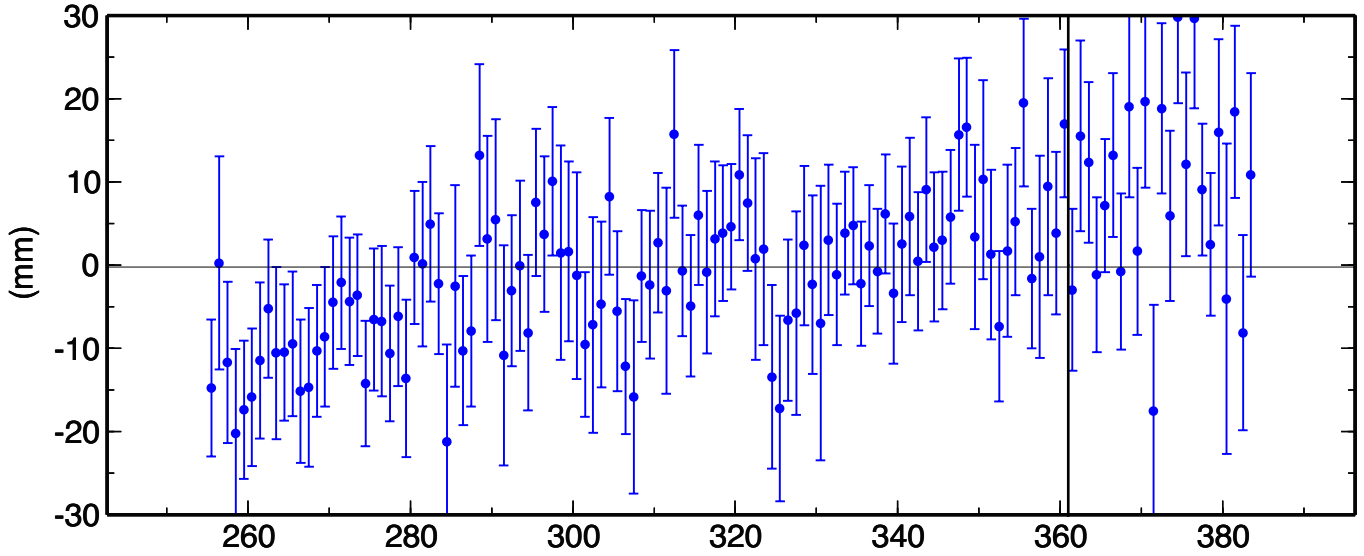

E

SAMP North Offset 403155.621 m

wmean(mm)= 5900.95 ± 0.53 nrms= 2.05 wrms= 7.1 mm # 43

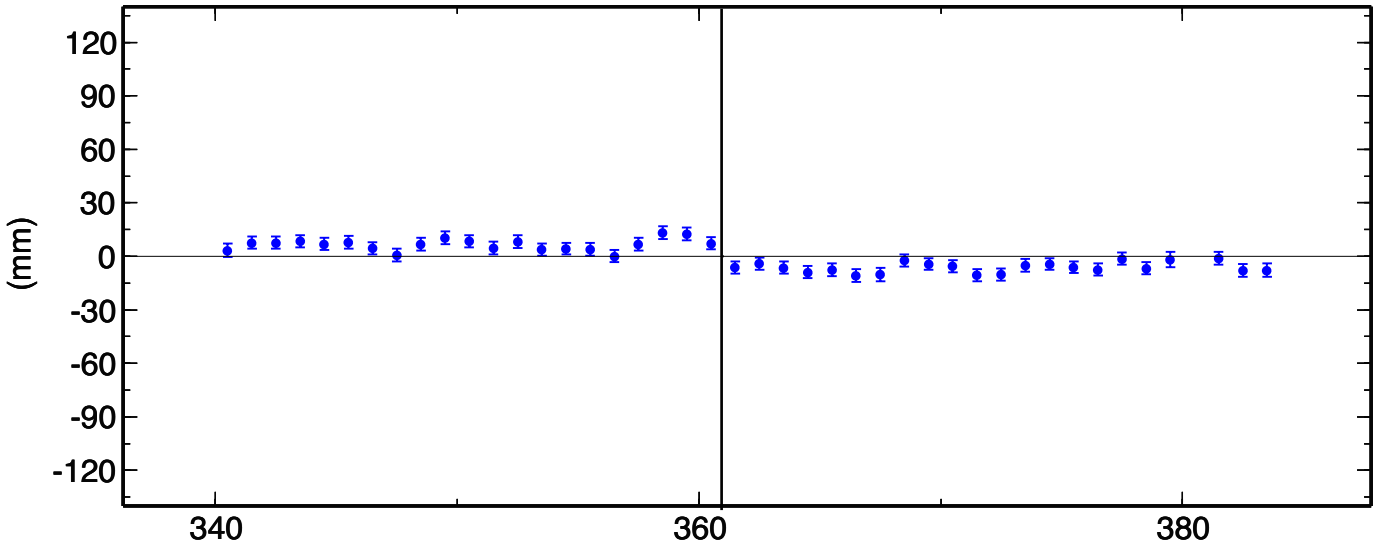

SAMP East Offset 10966936.079 m

wmean(mm)= 5977.01 ± 1.44 nrms= 7.61 wrms= 71.6 mm # 43

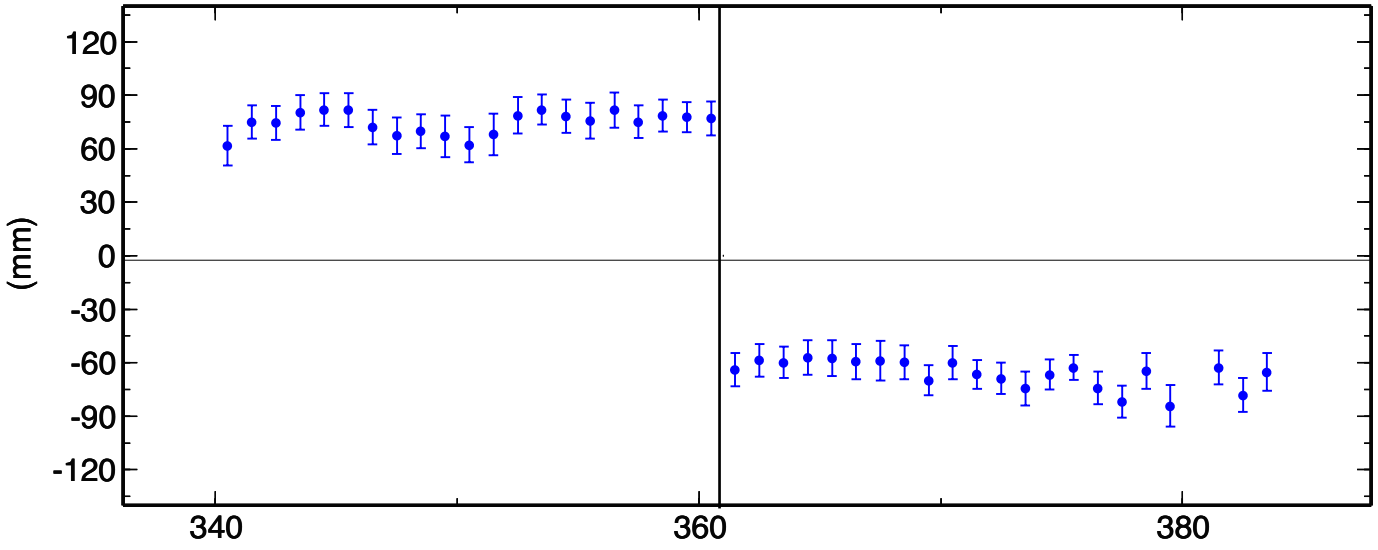

SAMP Up Offset 1.273 m

wmean(mm)= 1926.82 ± 2.94 nrms= 0.86 wrms= 16.7 mm # 44

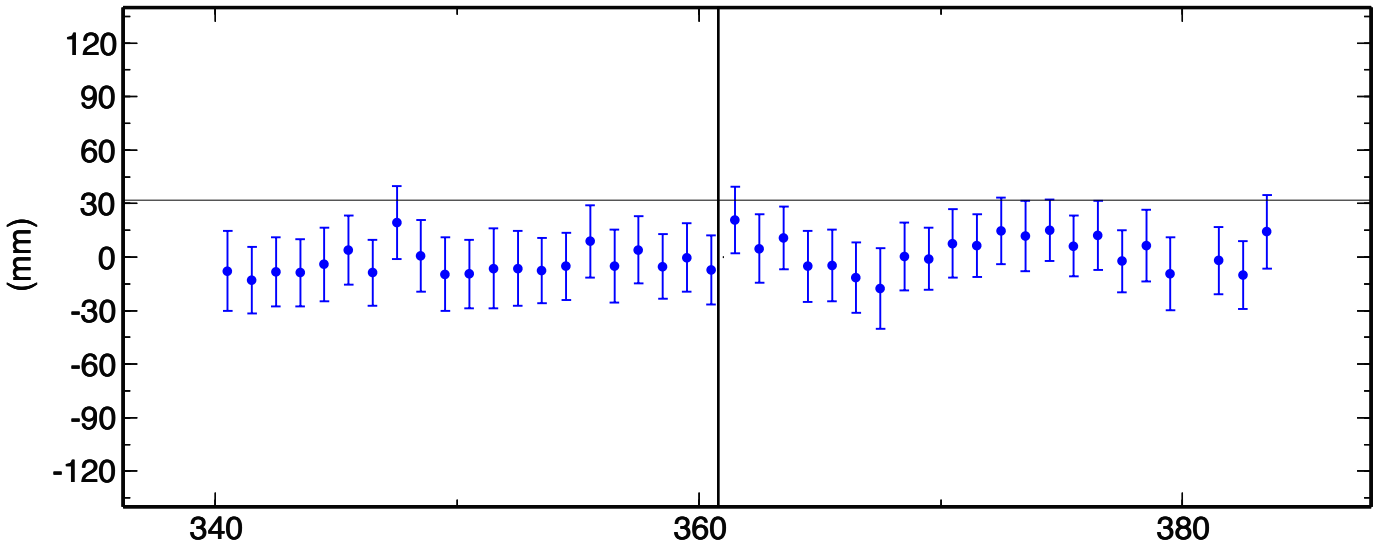

ITRF2000 reference stations

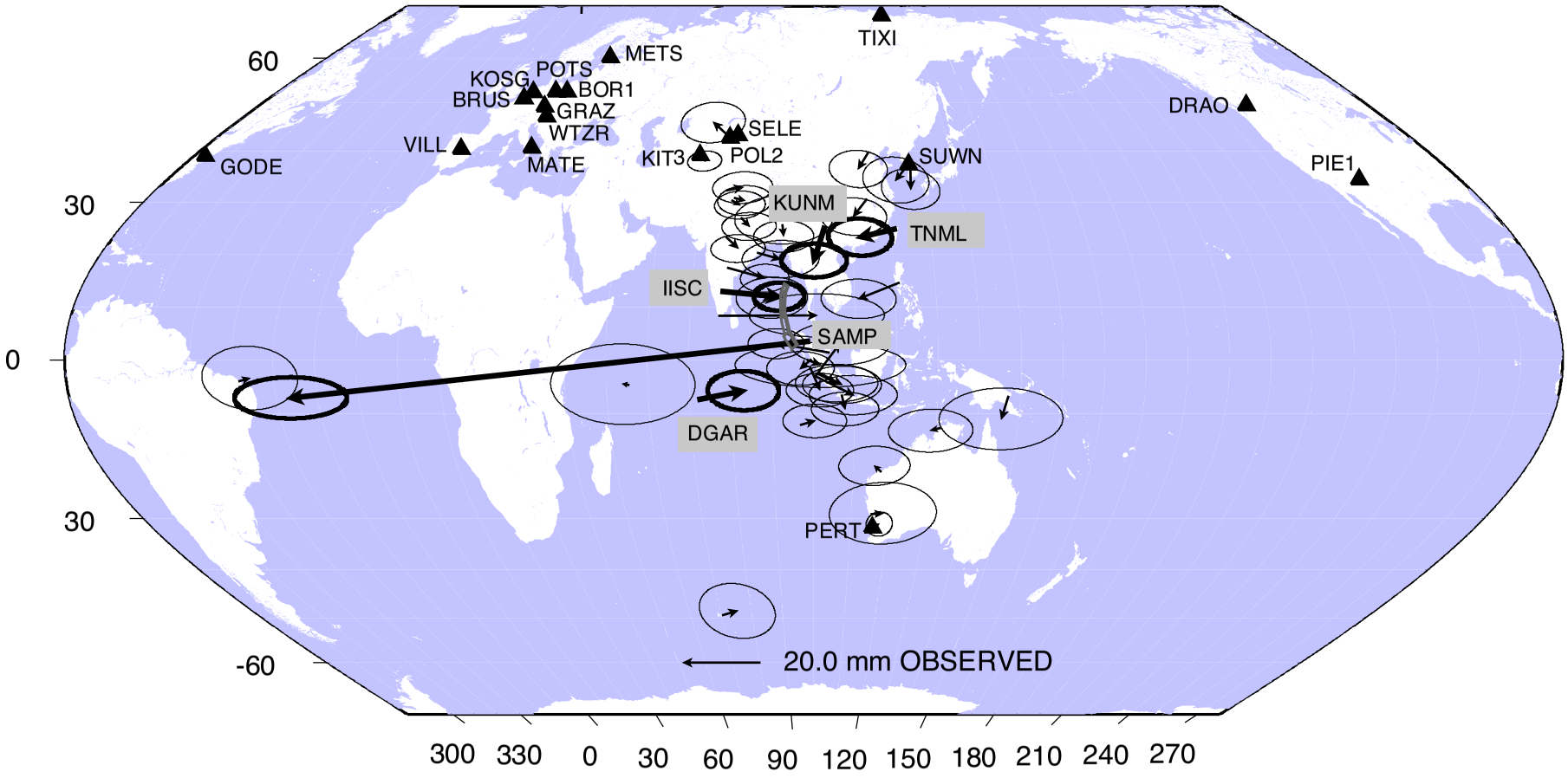

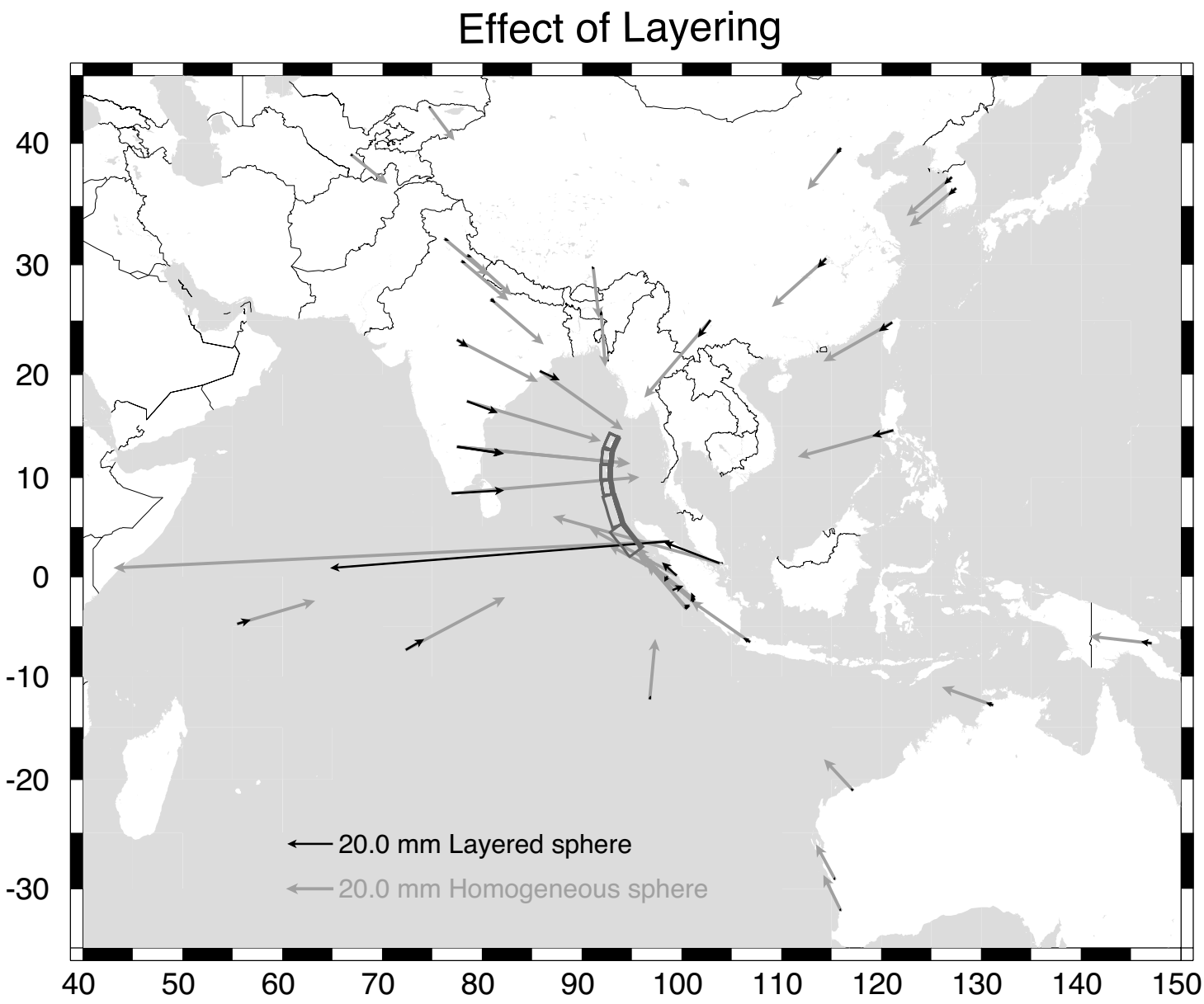
Effect of Layering
40
30
20
10
0
-10
-20
-30
40
50
60
70
80
90
100
110
120
130
140
150
20.0 mm Layered sphere
20.0 mm Homogeneous sphere

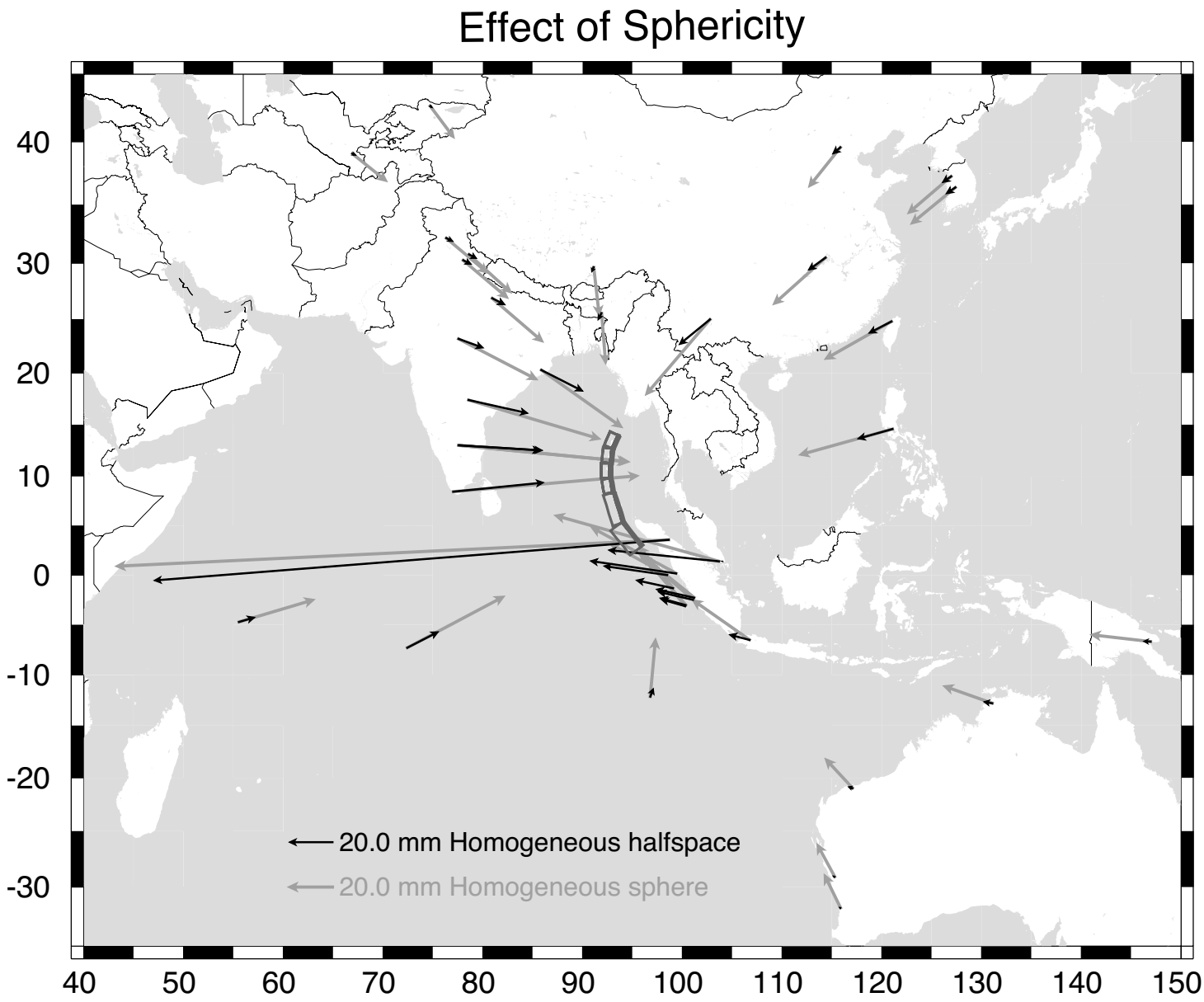
Effect of Sphericity
40
30
20
10
0
-10
-20
-30
40
50
60
70
80
90
100
110
120
130
140
150
20.0 mm Homogeneous halfspace
20.0 mm Homogeneous sphere

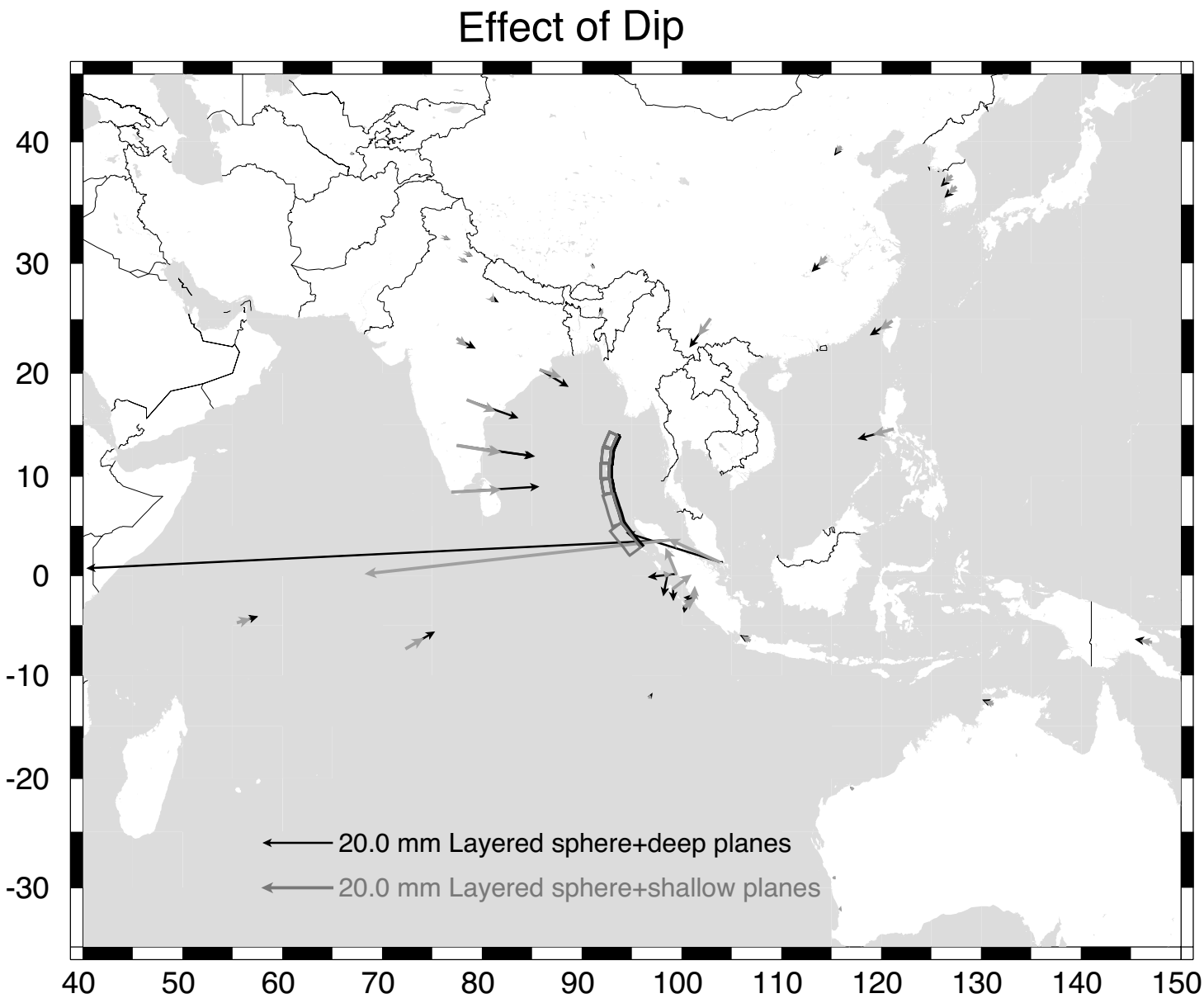
Effect of Dip
40
30
20
10
0
-10
-20
-30
40
50
60
70
80
90
100
110
120
130
140
150
20.0 mm Layered sphere+deep planes
20.0 mm Layered sphere+shallow planes

Supporting tables

Table S1. GPS measured coseismic horizontal surface displacements and their 1-sigma uncertainties estimated by differencing 5-day-average positions from before and after the earthquake, respectively. The average uncertainties of the measured offsets are 3.5 mm, 2.0 mm and 9 mm in the E, N and vertical components, respectively. The last two columns indicate which GPS data were in solutions provided by the Scripps Orbital and Permanent Array Center (http://sopac.ucsd.edu), which were included in our own processing, and those sites included in both solutions.

Table S2. Fault geometry parameters of coseismic model rupture planes.

Table S-1: GPS measured coseismic horizontal surface displacements and their 1-σ uncertainties

Lat °N	Lon °E	E_{offset} mm	N_{offset} mm	E_{sig} mm	N_{sig} mm	Site	Local solution	SOPAC solution
99.4	0.2	-2.8	-2.4	3.6	1.8	ABGS	*	
106.8	-6.5	0.9	-3.7	3.6	1.8	BAKO	*	*
77.5	13.0	13.1	-1.7	3.8	2.2	BAN2		*
78.6	30.8	2.8	-0.7	2.9	1.6	BHTW	*	
85.8	20.3	6.1	-1.7	4.1	2.0	BHUB	*	
115.9	39.6	-3.0	-4.2	3.1	2.0	BJFS		*
100.3	-3.1	6.5	8.7	5.3	2.3	BSAT†	*	
96.8	-12.2	3.7	1.1	3.4	1.8	COCO		*
127.4	36.4	-0.8	-5.3	3.1	2.2	DAEJ		*
131.1	-12.8	-2.5	-0.6	4.5	2.3	DARW		*
72.4	-7.3	11.5	2.2	3.8	2.1	DGAR	*	*
321.6	-3.9	2.9	0.8	5.1	3.4	FORT		*
78.5	17.4	9.9	-2.7	2.6	1.5	HYDE	*	*
77.6	13.0	14.9	-1.4	2.7	1.5	IISC	*	*
117.1	-21.0	-1.8	1.5	3.8	2.1	KARR		*
70.3	-49.4	4.2	1.2	4.0	3.0	KERG		*
66.9	39.1	1.6	-1.5	1.8	1.1	KIT3	*	*
102.8	25.0	-2.8	-8.5	3.5	1.8	KUNM	*	*
147.0	-6.7	-1.5	-6.0	6.6	3.3	LAE1		*
91.1	29.7	1.0	-4.2	5.2	2.6	LHAS	*	*
101.2	-2.3	6.1	-3.2	4.2	2.0	LNNG	*	
80.9	26.9	2.3	-2.2	2.9	1.5	LUCK	*	
101.1	-2.5	4.8	-2.5	4.4	2.0	MKMK	*	
99.1	-1.3	2.6	-6.0	3.6	1.8	MSAI	*	
76.3	32.2	4.0	0.8	3.2	1.7	NADI	*	
103.7	1.4	-13.8	2.4	3.0	1.6	NTUS	*	*
98.5	0.0	3.4	-1.2	9.1	2.4	PBAI‡	*	
115.9	-31.8	1.8	1.0	1.4	1.3	PERT		*
121.1	14.6	-10.8	-4.2	4.0	2.1	PIMO		*
74.7	42.7	-5.0	4.0	3.4	2.2	POL2	*	*
100.4	-3.0	9.9	-4.9	4.7	2.1	PRKB	*	
77.5	23.2	3.4	-2.9	2.9	1.5	RRLB	*	
98.7	3.6	-135	-14.8	6.0	2.2	SAMP	*	
55.5	-4.7	-1.6	0.3	7.7	4.3	SEY1		*
91.9	25.6	0.4	-3.0	3.2	1.7	SHL2	*	
127.0	37.3	-3.9	-4.1	3.5	2.5	SUWN		*
77.0	8.4	25.6	0.1	7.2	2.3	TIR0	*	
121.0	24.8	-9.2	-2.1	3.4	2.0	TNML		*
78.0	30.3	2.2	-1.2	2.7	1.5	WIH2	*	
114.4	30.5	-3.8	-4.5	3.5	2.0	WUHN		*
115.3	-29.1	3.1	0.2	5.7	3.3	YAR2		*

† Offsets at BSAT were calculated using means of data collected on days 350-354 and 375-379.

‡ Offsets at PBAI were calculated using means of data collected on days 350-354 and 370-374.

Table S-2. Fault geometry parameters of coseismic rupture planes

Segment	Endpoint[§]	$d_1^{\dagger}$	$d_2^{\ddagger}$	Rake	Length	Width	Strike*	Dip
		km	km		km	km	∘	∘
1	13.93°N 93.90°E	50	30	$\lambda_1 + 34°$	162.5	34.9	24	35
	12.65°N 93.20°E	50	30	$\lambda_1 + 17°$	162.5	34.9	7	35
	11.26°N 92.99°E	50	30	$\lambda_1 + 10°$	162.5	34.9	0	35
	9.79°N 92.99°E	50	30	λ_1	162.5	34.9	350	35
	14.01°N 93.55°E	30	0	$\lambda_1 + 34°$	162.5	97.1	24	18
	12.68°N 92.94°E	30	0	$\lambda_1 + 17°$	162.5	97.1	7	18
	11.26°N 92.73°E	30	0	$\lambda_1 + 10°$	162.5	97.1	0	18
	9.75°N 92.73°E	30	0	λ_1	162.5	97.1	350	18
2	8.40°N 93.30°E	50	30	λ_2	355	34.9	343	35
	8.33°N 93.05°E	30	0	λ_2	355	115.9	343	15
3	5.51°N 94.13°E	50	30	λ_3	350	34.9	322	35
	5.35°N 93.93°E	30	0	λ_3	350	157.2	322	11

All subsegments belonging to a segment are assumed to rupture with identical uniform slip. Variable rake is specified on the Andaman (segment 1) subsegments of variable strike such that absolute slip direction is kept constant. For a subsegment with strike ϕ and dip δ, the rake λ theoretically obeys the relationship

$\phi - 350° = \tan^{-1}(\tan\lambda\cos\delta) - \xi$, where ξ is the azimuth of the slip direction. For simplicity we adopt the approximation $\phi - 350° = \lambda - \lambda_1$.

§ Latitude and longitude of northernmost point on lower edge.

† Lower fault edge depth; ‡ Upper fault edge depth.

∗ Segment strike in degrees clockwise from due North.

Supporting references and notes

S1. R. W. King, Y. Bock, *Mass. Instit. of Tech., Scripps Inst. Oceanogr., Release 10.0* (2002).

S2. T. A. Herring, *Mass. Instit. of Tech.* (2002).

S3. F. F. Pollitz, *Geophys. J. Int.* **125**, 1-14 (1996).